nature communications

Article

https://doi.org/10.1038/s41467-024-54386-9

Fluorescent robust photoactuator via photo-crosslinking induced single-layered janus polyimide

Received: 28 May 2024

Accepted: 5 November 2024

Shuyu Xue[1,2,3], Zhipanxin Shi[1], Zaiyu Wang[3,4], Haozhe Tan[3], Feng Gao[3], Zicong Zhang[3], Ziyue Ye[3], Shifeng Nian[1], Ting Han[5], Jianbo Zhang[1,2] ✉, Zheng Zhao[3] ✉, Ben Zhong Tang[3,4] ✉ & Qiuyu Zhang[1,2] ✉

Advanced smart polymer materials with the ability of reversible deformation under external stimuli hold great potential in robotics, soft machines, and flexible electronics. However, the complexity and low efficiency for fabricating actuators along with their limited functionality hinder further progress. Here an efficient and mild catalyst-free thiol-yne click polymerization was developed to fabricate photosensitive polyimide (PI) films. Then the fluorescent robust photoactuators with single-layered janus structure were directly obtained via UV assisted photo-crosslinking of the films, exhibiting reversible response driven by a pronounced mismatch in expansion between the front and back sides of the films. Achieving selective, non-uniform spatial distribution within the PI films, rapid and reversible complex morphing of the actuators, along with the capabilities for encrypting, reading, and erasing fluorescent information—all through the use of a single UV light source—becomes straightforward. The robust mechanical property and driving ability of these actuators enable the conversion of light energy into obvious motion even under heavy loads and the leaping through the storage and release of energy, ensuring their potential for practical applications that require durability and reliability.

Smart materials that are capable of reversible deformation under external stimuli (e.g., heat, light, or magnetic field) have attracted tremendous attention due to their crucial applications in artificial muscles, soft actuators, robotics, and energy generators[1–7]. Substantial efforts have been dedicated to fabricating multi-functional advanced actuators, focusing on material design and mechanism exploration[8–12]. Among various materials, liquid crystalline elastomers (LCEs)[13–16] are particularly notable owing to their high tendency toward actuation derived from molecular order-disorder phase transition of the mesogens[17–19]. A critical prerequisite for the actuation of LCEs is mesogen alignment, followed by fixation through chemical cross-linking[20]. Conventional alignment methods such as mechanical

---

[1]School of Chemistry and Chemical Engineering, Key Laboratory of Special Functional and Smart Polymer Materials of Ministry of Industry and Information Technology, Northwestern Polytechnical University, Xi'an, Shaanxi, China. [2]School of Chemistry and Chemical Engineering, Key Laboratory of Material Physics and Chemistry under Extraordinary Conditions of Ministry of Education, Northwestern Polytechnical University, Xi'an, Shaanxi, China. [3]School of Science and Engineering, Shenzhen Institute of Aggregate Science and Technology, The Chinese University of Hong Kong, Shenzhen (CUHK-Shenzhen), Guangdong, China. [4]Department of Chemistry, Hong Kong Branch of Chinese National Engineering Research Center for Tissue Restoration and Reconstruction, The Hong Kong University of Science and Technology, Kowloon, Hong Kong, China. [5]Center for AIE Research, Shenzhen Key Laboratory of Polymer Science and Technology, Guangdong Research Center for Interfacial Engineering of Functional Materials, College of Materials Science and Engineering, Shenzhen University, Shenzhen, China. ✉e-mail: zhangjb@nwpu.edu.cn; zhaozheng@cuhk.edu.cn; tangbenz@cuhk.edu.cn; qyzhang@nwpu.edu.cn

stretching or rubbed surface confinement typically result in simple planar contraction or expansion[7,21]. In order to achieve more complicated shape morphing, elevated demands are put forward on both polymers and alignment methods to disrupt the symmetric distribution of the monodomain in LCEs. For instance, introducing photosensitive groups in LCEs enables the establishment of actuators with spatially distributed domains of actuation through photo-induced crosslinking[7,22]. If cross-linking occurs only in monodomain of the superficial layer, while the rest of the film remains in an isotropic state or polydomain, the film bends upon stimulation. Besides, UV-patterned crosslinking using photomasks endows more complex motion such as waving and wrinkle[22]. Despite offering an unusual versatility, the usually demanding synthesis of photosensitive LC polymers and the complexity of alignment methods undoubtedly limit their applications. It is thus challengeable but highly desired to develop a direct approach to fabricate programmable actuators without the necessity of organizing the mesogen alignment.

Beyond the aim of achieving simplicity and efficiency in developing advanced actuators with customizable movement, the choice of stimulus and the multifunctionality of actuators also merit special attention. Remarkably, light not only spatially tunes the distribution of alignment of mesogens[23], but also stands out as an ideal stimulus for shape morphing of actuators due to the unique capability of photomechanical materials to directly convert light energy to mechanical work, facilitating wireless, directional, remote and spatial control[19,24,25]. Typically, the light-induced deformation of a single material is often achieved by introducing azobenzene into polymers[18,26,27]. Through thoughtful design of the polymer structure, the trans-cis photoisomerization of azobenzene can magnify molecular motions to macroscopic deformation under light irradiation. Yet, azobenzene-containing single materials always require the operation of dual wavelength (UV and visible light) for reversible actuation[18,28], showing poor driving performance when compared to lamellar or composite actuators using only one beam of UV light[29–31]. The realization of rapid and reversible actuation with a single wavelength of light still necessitates further breakthroughs. An additional advantage of light stimulus lies in its capacity to enrich the materials with diverse functionalities. Fluorescence, visible only under light irradiation, offers significant superiority in information encryption, protection, and customized fluorescent patterns[32–35]. When integrated with photoactuators, advanced functions such as position tracing and information transmission can be achieved simultaneously during light-driven actuation. This concept parallels the behavior of some intelligent living organisms, for instance, mimicry octopus not only rapidly changes shape when stimulated, but also displays patterns on its body to imitate other creatures, so as to achieve the purpose of intimidation or attraction. Thus, in future studies, integrating these multifaceted capabilities into one single system in a simple way is preferable, which will broaden the scope and versatility of smart photoactuators to emulate a large number of functions observed in nature.

From the above overview, utilizing light as a tool presents a straightforward and convenient approach across multiple synergistic polymer materials to achieve one particular function. This prompts an intriguing question: is there an all-in-one strategy to integrate these advanced functions into one single material exclusively utilizing a single wavelength of light, concurrently achieving non-uniform optical inscription, information transmission and fast reversible motion? Regrettably, the exploration into such versatile materials remains limited. Due to the suffering of inflexible and cumbersome mesogen alignment, as well as the common problem of poor mechanical property with soft materials[21,36], LCEs or hydrogels are not the first choice. Moreover, limited by the monotonous property of most individual material, it is also difficult to afford a single material that is capable of rapid and reversible large deformation using light at one wavelength without relying on auxiliary molecules or materials. Furthermore, for practical applications in diverse high-tech areas, higher demands are placed on the strength, modulus, heat resistance and weathering resistance of smart materials[37,38]. It is evident that this endeavor is challenging but holds considerable allure.

To solve this challenge, herein a fabrication strategy towards multifunctional actuators is proposed through a single-layered janus polyimide (PI) film characterized by robustness and photo-crosslinking capability. The concept is based on a serious mismatch in expansion between the front and back sides of a single PI film to achieve fast reversible response, which is different from the photomechanical deformation in azobenzene-functionalized PIs reported before[39,40]. First, high molecular weight PIs containing photosensitive double bonds were efficiently synthesized at 30 °C in 15 min by the developed catalyst-free thiol-yne click polymerization (Fig. 1a). The actuators were then fabricated by photo-crosslinking the front side of PI thin films (10 μm thickness). As the light intensity decreases with the penetration depth owing to absorption and scattering[41], the irradiated region was induced to gradient degree of crosslinking from the surface to the interior, producing a serious mismatch in thermal expansion along the thickness direction. The rapid photoresponse is attributed to a certain photothermal effect of ultrathin actuator under UV light, thus obtaining a walking robot. Moreover, introducing aggregation-induced emission luminogens (AIEgens) into polymers not only allows for location tracking of actuator, but also generates interesting photo-enhanced fluorescence property that enables information coding on actuators. When spatial heterogeneity is performed under a photomask upon UV irradiation, fluorescent patterns or letters can be encrypted on the surface of actuator simultaneously. The combination of light-driven three-dimensional (3D) actuation with the encryption, reading and erasure of fluorescent messages establishes a dynamic "dimension" for enhancing information safety. Crucially, localized actuations through programmed photo-crossing of PI films in selected regions can be easily realized to enable waving motion, showing the flexibility of our strategy. The robust mechanical properties of the films ensure that, even under load, they still support light-controlled rapid and reversible actuation to simulate some machines for valuable engineering applications, such as weightlifting, throwing and load movement.

Results

Preparation of PIs

A highly efficient and gentle thiol-yne click polymerization was developed to prepare programable PIs (Fig. 1a). The preparation of the two polymeric monomers is simple, in which the diynes 6FDA-APA and BPADA-APA are prepared by the reaction of two commercially available dianhydrides 4,4′-(hexafluoroisopropylidene) diphthalic anhydride (6FDA) and 2,2-bis[4-(3,4-dicarboxyphenoxy) phenyl]propanedianhydride (BPADA) with 3-ethynylaniline in one step. Similarly, the dithiol 6FSH is also prepared in one step from two commercially available 6FDA and 4-aminothiophenol (Supplementary Fig. 1). In order to realize solid state fluorescence, tetraphenylethylene (TPE), a protype AIEgen-containing diyne (TPE-APA) was designed for the synthesis of PIs with UV-responsive fluorescence property (Supplementary Fig. 2). A model compound was also synthesized shown in Supplementary Fig. 3. By optimizing the polymerization conditions, it was found that the polymerization between imide-containing dithiol with imide-containing diynes could be completed without any catalyst in just 15 min at 30 °C, yielding PIs with high molecular weights up to 126 kDa (Fig. 1a, Supplementary Tables 1–2, Supplementary Figs. 4–6). Notably, the rational structure design promoted an anti-Markovnikov monoaddition pathway of the monomers, preserving photosensitive double bonds in the main chain for spatial manipulation. This powerful catalyst-free thiol-yne click polymerization provides a way for the preparation of linear mono-addition polymers. The structures of the monomers and resulting PIs have been characterized by FT-IR and

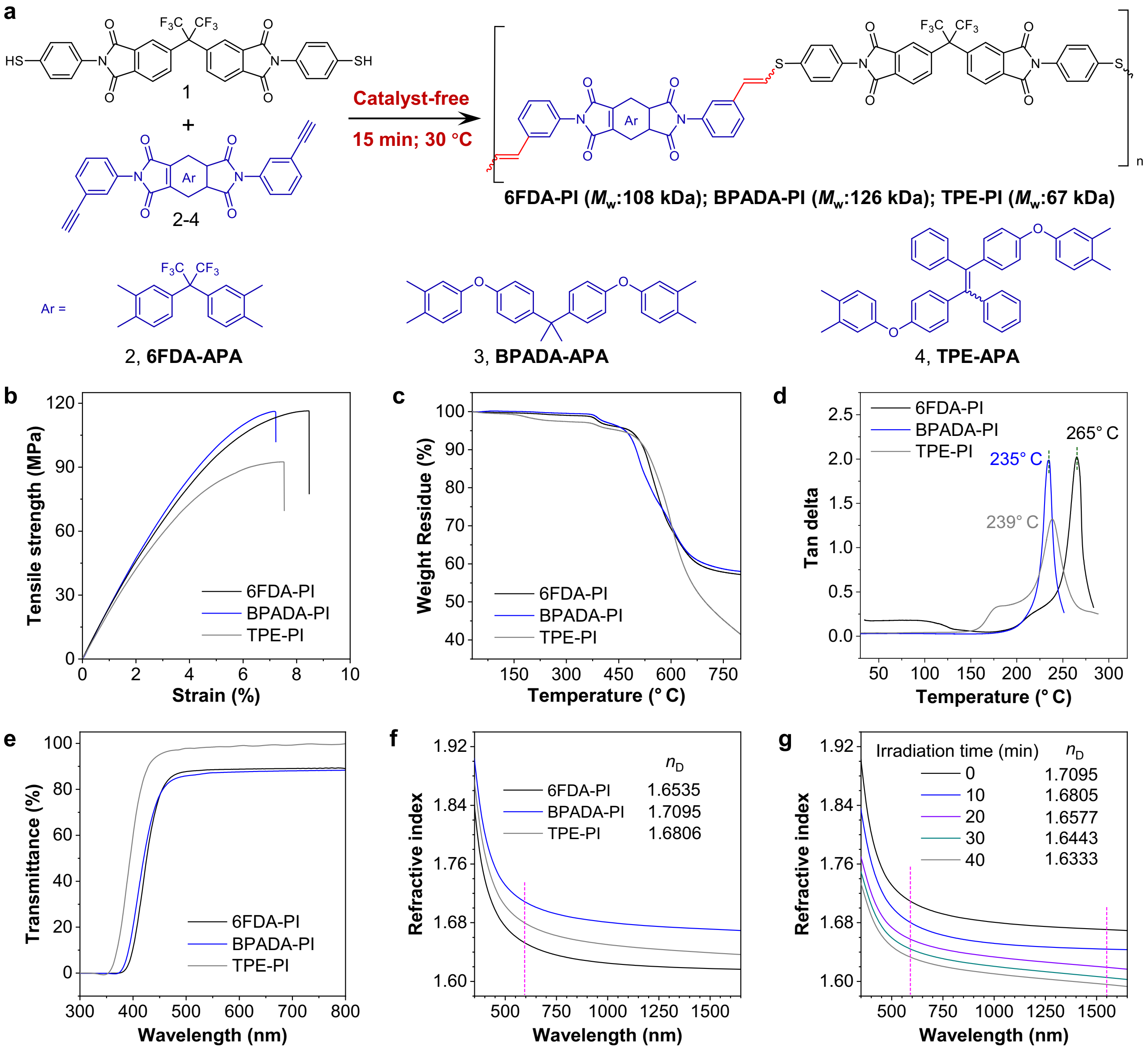

Fig. 1 | Preparation and characterization of the PIs. a Synthetic route for the photoresponsive PIs via catalyst-free thiol–yne click polymerization between imide-containing dithiol **1** with diynes **2**-**4**. **b** Typical stress-strain curves of the PI films. **c** TGA (thermal gravimetric analyses) curves of the PIs from room temperature to 800 °C under nitrogen atmosphere. **d** DMA (dynamic mechanical analyses) curves of the prepared PI films: tan delta versus temperature. **e** Transmittance curves in visible light region of the resulting PI films (~10 µm). **f** Wavelength dependence of refractive indices of thin films. Abbreviation: n_D = refractive index at 589.2 nm. **g** Change in the refractive index of **BPADA-PI** by UV irradiation for different durations.

nuclear magnetic resonance (Supplementary Figs. 7–26). All PIs exhibit an amorphous-like morphology with a broad peak (Supplementary Fig. 27). Benefit from the desirable solubility (Supplementary Table 3), the resulting PIs can be cast into robust self-standing thin films (Supplementary Fig. 28). The mechanical, thermal and optical properties of PI films were evaluated. The tensile strength and moduli are in the range of 94.1–116.2 MPa and 2.1–2.6 GPa, respectively (Fig. 1b, Supplementary Table 4). Despite the preference for high mechanical properties in engineering applications, this also presents a challenge in designing photo-driven actuators, as a stiff matrix always suffers severely limited motion than soft matrix[37]. We later demonstrate the effects of material thickness and UV irradiation time on driving performance. The thermal stability and thermomechanical properties of optical actuators are critical for their high temperature applications. Most thiol-based click polymers suffer from 5% weight loss temperature ($T_{5\%}$) below 450 °C, attributed to the labile thioether in their backbone[42]. However, by incorporating aromatic imide rings and trifluoromethyl groups into the main chain of polymers, the obtained PIs show high $T_{5\%}$ in the range of 452–482 °C and $T_{10\%}$ in the range of 500–528 °C (Fig. 1c), surpassing those of analogous polymers reported previously[43]. Besides, the incorporation of imide moiety also promises a robust and rigid polymer network with high glass transition temperatures (T_g) ranging from 235 to 265 °C, showing superior thermal properties compared to LCEs (Fig. 1d and Supplementary Fig 29). The highest T_g, reaching up to 265 °C, is observed in 6FDA-PI, presumably due to the highly rigid structure of 6FDA-based diyne. The isopropyl and flexible ether linkages of BPADA-APA are responsible for the lowest T_g of BPADA-PI. The UV–vis optical transmission spectrum (Fig. 1e) reveals that several PI films with light-yellow color have strong UV absorption in a wavelength range of <400 nm. Owing to the introduced sulfur atoms with strong atomic polarizability, all PI films exhibit high refractive index (n) ranging from 1.6806 to 1.7095 at

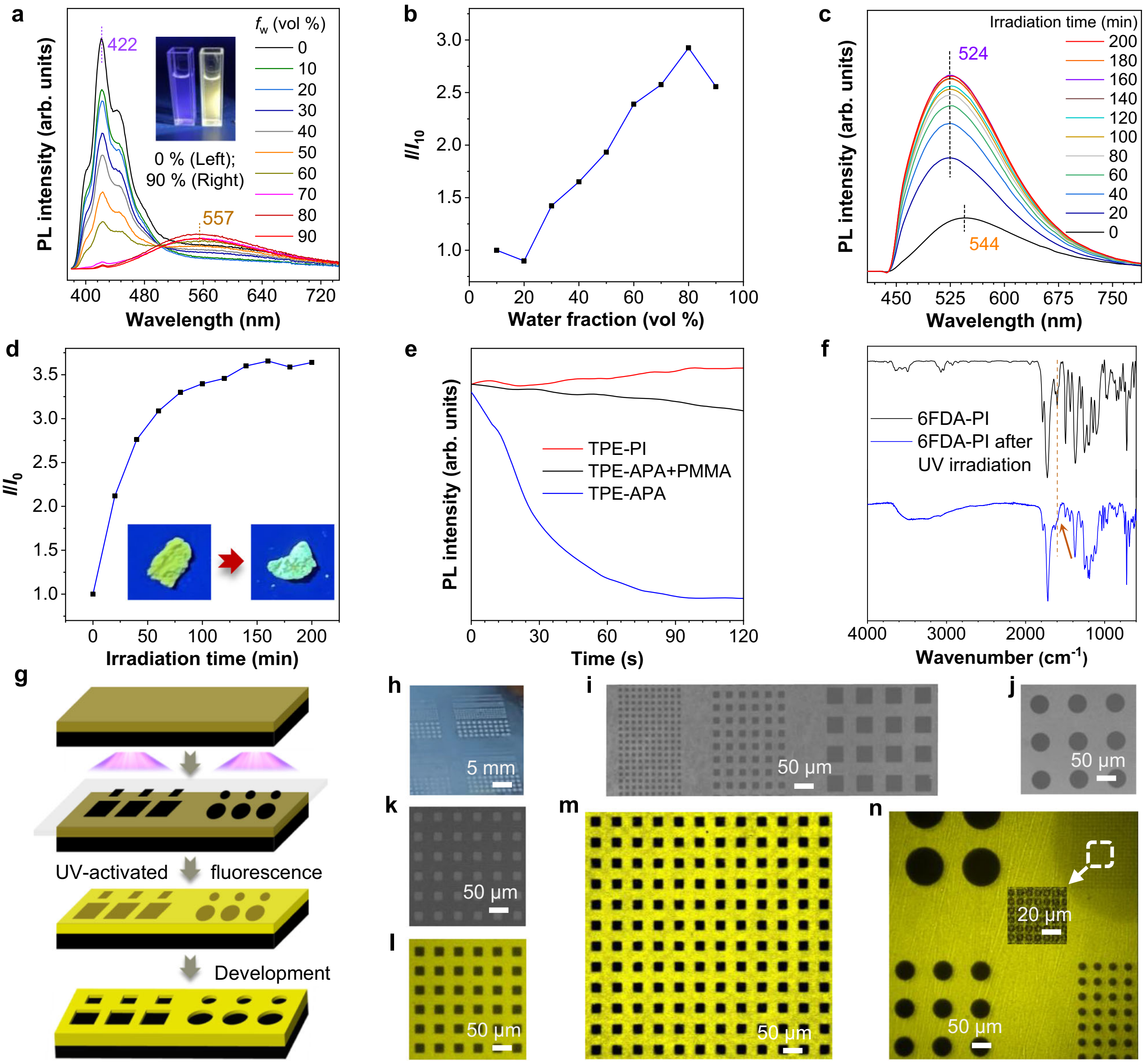

Fig. 2 | Characterization of the TPE-based monomer, PIs and their photopatterns. a Photoluminescence (PL) spectra of TPE-PI in THF and THF/water mixtures with different water fractions (f_w). Solution concentration: 100 μM. Inset: the corresponding fluorescent photographs. **b** Plot of relative PL intensity (I/I_{10}) at 557 nm for TPE-PI versus the composition of the THF/water mixture. **c** PL spectra of the TPE-PI powder upon UV irradiation (365 nm, 100 mW cm^{-2}), **d** Plot of relative PL intensity (I/I_0) at 544 nm versus irradiation time. Inset: fluorescent images of the TPE-PI powder before and after irradiation with UV light for 200 min. **e** Real-time monitoring of fluorescence intensity change of TPE-PI, TPE-APA and TPE-APA /PMMA films with irradiation time (405 nm). **f** FT-IR spectra of the 6FDA-PI powder before and after UV irradiation. **g** Schematic illustration of the fabrication of 2D and 3D photopatterns. **h** Photograph of negative photoresist on silicon wafer. **i**, **j** 3D patterns with different sizes and shapes from 6FDA-PI. **k** 2D photopatterns from TPE-PI taken under normal room light. **l** 2D fluorescent photopattern from TPE-PI taken under 405 nm using a fluorescent microscope. **m** 3D fluorescent photopatterns of TPE-PI taken under 405 nm using a fluorescent microscope. **n** 2D fluorescent photopatterns of TPE-PI with different sizes taken under 405 nm using a fluorescent microscope.

598 nm (Fig. 1f, Supplementary Table 5), much higher than those of the commercially optical polymers ($n < 1.65$)[44]. Moreover, the n values of the obtained PIs are responsive to UV irradiation. Figure 1g shows the n value of BPADA-PI at 589 nm greatly decreases with increasing UV exposure time (from 1.7095 to 1.6333 upon exposure for 40 min). The good tunability comes from the structural changes generated by the photosensitive double bonds of the PI backbone, showing potential applications in gradient-index optics[45].

The absorption and photoluminescence (PL) properties of the monomer TPE-APA and PIs were studied in their THF solutions and THF/water mixture with different water fractions (f_w) (Supplementary Figs. 30–34). The pure solution of TPE-APA was non-emissive (Supplementary Fig. 31), but when poor solvent of water was added into the THF solution, the emission was increased dramatically when water fraction exceeds 70%, displaying a typical AIE effect. Since TPE-APA is AIE active, we expect that the polymer obtained by polymerization of TPE-APA with dithiol retains the AIE characteristics. As depicted in Fig. 2a, the pure THF solution of TPE-PI exhibited blue-violet fluorescence emission with λ_{em} at 422 nm. When increasing the amount of water added into the THF solution, the PL intensity at 422 nm decreases dramatically. It is noteworthy that another emission peak at 557 nm is observed clearly with the increasing of water and the intensity increases at water fraction larger than 20%, exhibiting AIE feature (Fig. 2b). However, the 6FDA-PI without TPE in main chain exhibits gradually decreased emission upon aggregation (Supplementary Fig. 32). Obviously, the emission at 557 nm of TPE-PI originated from aggregation. These results indicated that the AIE feature of the active core TPE was also well-preserved in TPE-PI. Typically, TPE-containing monomers or polymers suffered from UV-quenched fluorescence which was ascribed to the transformation of propeller-like TPE into more planar ACQ molecules through photocyclization[46,47]. Introducing TPE into the rigid PI matrix is anticipated to mitigate this effect. Figure 2c, d and Supplementary Fig. 35 display the fluorescence spectra of powder and film of TPE-PI before and after UV irradiation in oxygen atmosphere respectively. Amazingly, the emission peak of TPE-PI powder appeared at 544 nm, while the intensity of this peak increased upon UV light irradiation, exhibiting a special property of UV-activated fluorescence. After 140 min of irradiation, the emission intensity was 3.5-fold higher than the original level. Smooth TPE-PI thin films fabricated by spin-coating on silicon wafers showed similar phenomenon of UV-activated fluorescence (Supplementary Fig. 35). This phenomenon, which was different from the traditional TPE-containing polymers[45], prompts further investigation that whether the monomer TPE-APA had similar photoresponsive characteristics as polymer. A 405 nm laser was used to irradiate the films of TPE-PI, TPE-APA and TPE-APA/PMMA, respectively. As shown in Fig. 2e, TPE-PI film demonstrated UV-activated fluorescence property, which was consistent with the results obtained under UV lamp at 365 nm. However, the diyne monomer TPE-APA and the doped film of TPE-APA/PMMA showed UV-quenched fluorescence, among which the emission of pure film of TPE-APA decreased significantly while the doped film of TPE-APA/PMMA decreased slightly (Supplementary Fig. 36). This indicates that blending this monomer with PMMA significantly suppresses the fluorescence quenching of TPE by UV light. We further investigated the reason why TPE-PI exhibited photo-enhanced fluorescence while TPE-APA shows quenched fluorescence. Since three PIs completely dissolve in chloroform but become insoluble after exposure to UV light, we believe this is the result of the cross-linking reaction between photosensitive double bonds of the molecular backbone under UV light without additional initiators. The FT-IR spectra of polymer as well as model compound before and after UV light (Fig. 2f and Supplementary Fig. 37) confirmed the disappearance of the original peak of double bond after sufficient UV light. Therefore, UV-activated fluorescence of TPE-PI was attributed to the denser polymer network formed by double bond crosslinking, which further restricted the rotation of the phenyl rings of TPE, leading to the enhanced fluorescence. Polymers with good photosensitivity are capable of generating complex micro- and nanopatterns, which are highly desirable in the field of optical writing and reading, high-performance photonic devices, anti-counterfeiting applications and semiconductor manufacturing[45]. Due to the insolubility caused by polymer crosslinking after UV exposure, all three PI films could form stereolithography patterns on silicon wafer surface by simply exposing them to UV light in the presence of a copper photomask, followed by developing in solvent (Fig. 2g–j). The photopattern process underwent without any photoiniator and photocrosslinker. Besides, two-dimensional (2D) and 3D fluorescent patterns showing good photolithographic performance could be readily achieved using TPE-PI (Fig. 2k–n). It is worth noting that 2D patterns also remain visible under normal room light (Fig. 2k) probably because of the distinct change of the film refractivity upon UV irradiation[45]. After the photolithography process, the unexposed parts of the PI film still showed weak emission, while the emission of the exposed parts is significantly enhanced to give a turn-on-type 2D fluorescent photopattern with high resolution of 5 μm (circle, Fig. 2n). Beyond circle pattern, other patterns with different shapes and sizes could also be readily obtained and clearly visualized. After removing the soluble unexposed parts of the film with solvent as the developer, a well-resolved 3D negative fluorescent pattern is formed as shown in Fig. 2m.

Fabrication of PI-based actuators

Actuators were fabricated by simply placing the PI films containing photosensitive double bonds under an UV lamp and irradiating the front side (Fig. 3a). The light-driven performance of the actuators depends on the preparation conditions including UV irradiation intensity, irradiation time and the film thickness. Specifically, a 6FDA-PI film (≈10 μm thick) is placed under a UV lamp with a power of 100 mW cm^{-2} for gradient optical inscription and the maximum bending angle (θ) of the actuator gradually increases with prolonged irradiation time. After 30 min of irradiation, the resulting actuator bends 180 degrees within 3 s when exposed to UV light (Fig. 3b, c, Supplementary Movie 1). The length (L) of two ends of the film changes from 1.5 cm to 0.4 cm (Fig. 3d). Upon turning off the UV light, the actuator almost returns to its original shape. The bending process under UV light and the extension process without light can be repeated for many cycles (Fig. 3c), suggesting it could work as a reversible actuation. Notably, bending is always towards the front side of the film, regardless of the direction of UV irradiation. Photoactuators exhibit reversible photomechanical deformation when stimulated by light. It is important to understand the actuation mechanisms to achieve controllable mechanical deformation. Among photoactuators, light energy is mainly converted into thermal or chemical energy in actuating materials. Photothermal actuators are widely developed owing to their simple preparation and design principles[48,49]. Generally, they have a bi-layered or tri-layered structure and the actuation occurs due to a mismatch in the expansion between layers to achieve fast responses[50,51]. The driving mechanism of our current work is due to a mismatch of thermal expansion on two sides of the actuator, which is similar to reported bimorph photothermal actuators. The difference is that the actuator was efficiently prepared in one step by irradiating PI film containing photosensitive double bonds with ultraviolet light to form heterogeneity, which is simpler than a composite approach. As the light attenuation with the penetration depth owing to absorption and scattering, the obtained actuators have a gradient cross-linked single-layer structure (Fig. 3a) and there is no typical layer interface, which avoids the interface problems that may exist in multi-layer materials. A short irradiation time can't cause a significant difference in the crosslinking degree between the front and back side. The distinct difference between the two sides of one film after 30 min of irradiation is evidenced by the visual morphology captured by SEM images. It can be seen in Fig. 3e that the two sides of the untreated PI film have the same smooth surface morphology. However, after irradiation by UV lamp, microtraces appear on the front side, while the back side still remains smooth morphology (Fig. 3f). These microtraces have a width of about 100 nm and are spread across the entire front side of the film (Supplementary Fig. 38), indicating that the double bonds of the front side undergo cross-linking after irradiation. Due to insufficient penetration depth of UV light, the back side maintains their original smooth morphology. Therefore, we believe that the back side retains linear structure of polymer without cross-linking. Interestingly, benefiting from the correlation between fluorescence intensity and irradiation level of TPE-PI, the janus structure of the exposed film is further confirmed by the distinct difference in fluorescence intensity between the front and back sides. The fluorescence intensity on the front was significantly higher than that on the back side, presenting bright-yellow emission (Fig. 3g). While the back side retained a dark-yellow emission, consistent with the emission of the original film, which further confirmed the fact that the film produces a cross-linking gradient along the thickness after irradiation, with the highest cross-linking degree on the front side and none on the back side. The characterization of related structures was further proved by tests of thermal expansion on the films before and after UV treatment. If the film undergoes cross-linking after irradiation, the dimensional expansion rate should be lower than that of the original film. Since the actuator obtained by irradiating only one side of the film also responds to heat, the irradiated film can be

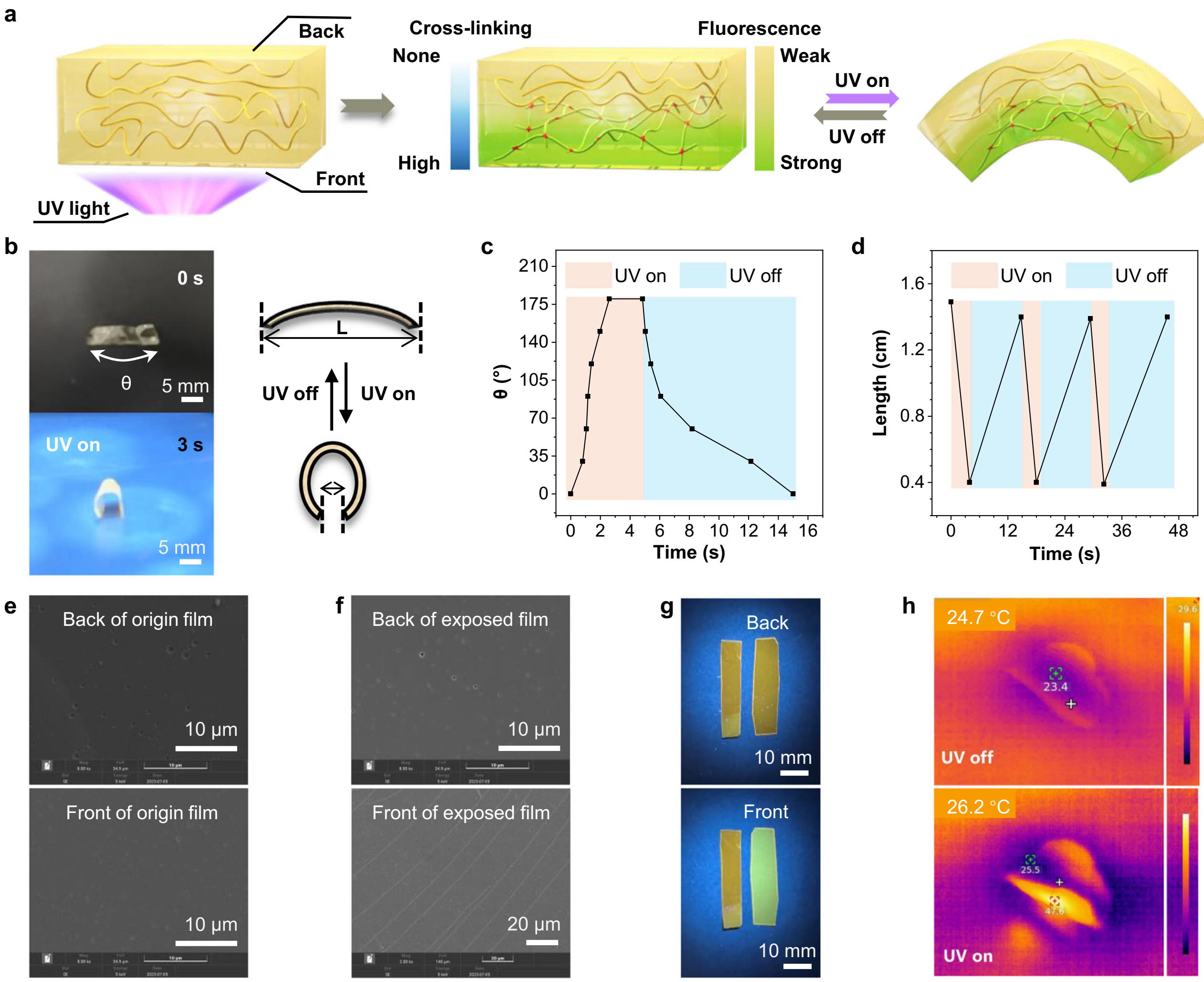

Fig. 3 | Fabrication and characterization of the photo-crosslinking induced single-layered janus PI films. a Schematic illustration of the fabrication process of the photo-driven PI films and the mechanism of the reversible actuation. **b** Photographs of an actuator based on 6FDA-PI driven by UV light. **c** Dependence of the bending angle (θ) on the operation time for 6FDA-PI film. **d** Dependence of the length (L) of two ends of 6FDA-PI film on the operation time. **e** SEM images of the front and back side of original 6FDA-PI film. **f** SEM images of the front and back side of exposed 6FDA-PI film. **g** (top) Photographs of original TPE-PI film (left) and the back side of exposed TPE-PI film (right) under UV lamp. (bottom), Photographs of original TPE-PI film (left) and the front side of exposed TPE-PI film (right) under UV lamp. **h** Infrared thermal images of a 6FDA-PI based actuator with and without UV light (100 mW cm^{-2}).

driven during the heating process, which affects the test results. Based on this consideration, both sides of the PI film were irradiated by the same condition (UV irradiation for 30 min, 100 mW cm^{-2}) to obtain the irradiated film. Then these films were heat treated, followed by a thermal mechanical analysis test and the results were shown in Supplementary Fig. 39. It could be seen that the original film gradually began to expand as the temperature increased from room temperature, while the irradiated film didn't expand significantly from 25 °C to about 45 °C. At about 45 °C, the dimensional deformation rate of the untreated film is nearly 5 times that of the irradiated film. Therefore, the actuators obtained by irradiating only one side of the film have a cross-linking gradient. The front of the film underwent intense UV-induced double bond crosslinking, the formed three-dimensional network structure resulted in a large extent of mismatch in thermal expansion between the two sides of the film, with the front exhibiting a smaller expansion than the back, which allowed the film to achieve deformation at a much lower temperature (40 °C) when placed on a heating table, as shown in Supplementary Fig. 40. A heating table at 80 °C resulted in larger deformation (Supplementary Fig. 41). Furthermore, Fig. 3h illustrated the temperature distribution along the 6FDA-PI film under UV light using infrared thermal images. Thanks to the lower deformation temperature, photo-activated deformation was achieved utilizing the photothermal effect of the PI film itself under lower power UV irradiation without the need for any photothermal reagents. Because this concept depends on light attenuation, the thickness of the PI film also plays a crucial role in affecting the reversible actuation. Firstly, three 6FDA-PI films of different thicknesses were prepared, which were 5 μm, 10 μm, and 20 μm respectively. These films were illuminated by UV light (intensity: 100 mW cm^{-2} for 30 min) to obtain photoactuators of different thicknesses. Then, the influence of thickness on actuating performance was studied under UV light of about 150 mW cm^{-2} (Supplementary Figs. 42 and 43). The results showed that the actuators (thickness 5 μm and 10 μm) can bend about 100° in approximately 800–1000 ms upon exposure to UV light. Continuously increasing the thickness to 20 μm, the actuating performance will be influenced. Therefore, the thickness of the actuators is better to smaller than 20 μm. The performance reduction may be assigned to that when a thicker film is irradiated to form heterogeneity, the thickness of the photo-crosslinked layer is basically the same as that of the thinner film, but the thickness of the uncrosslinked layer is

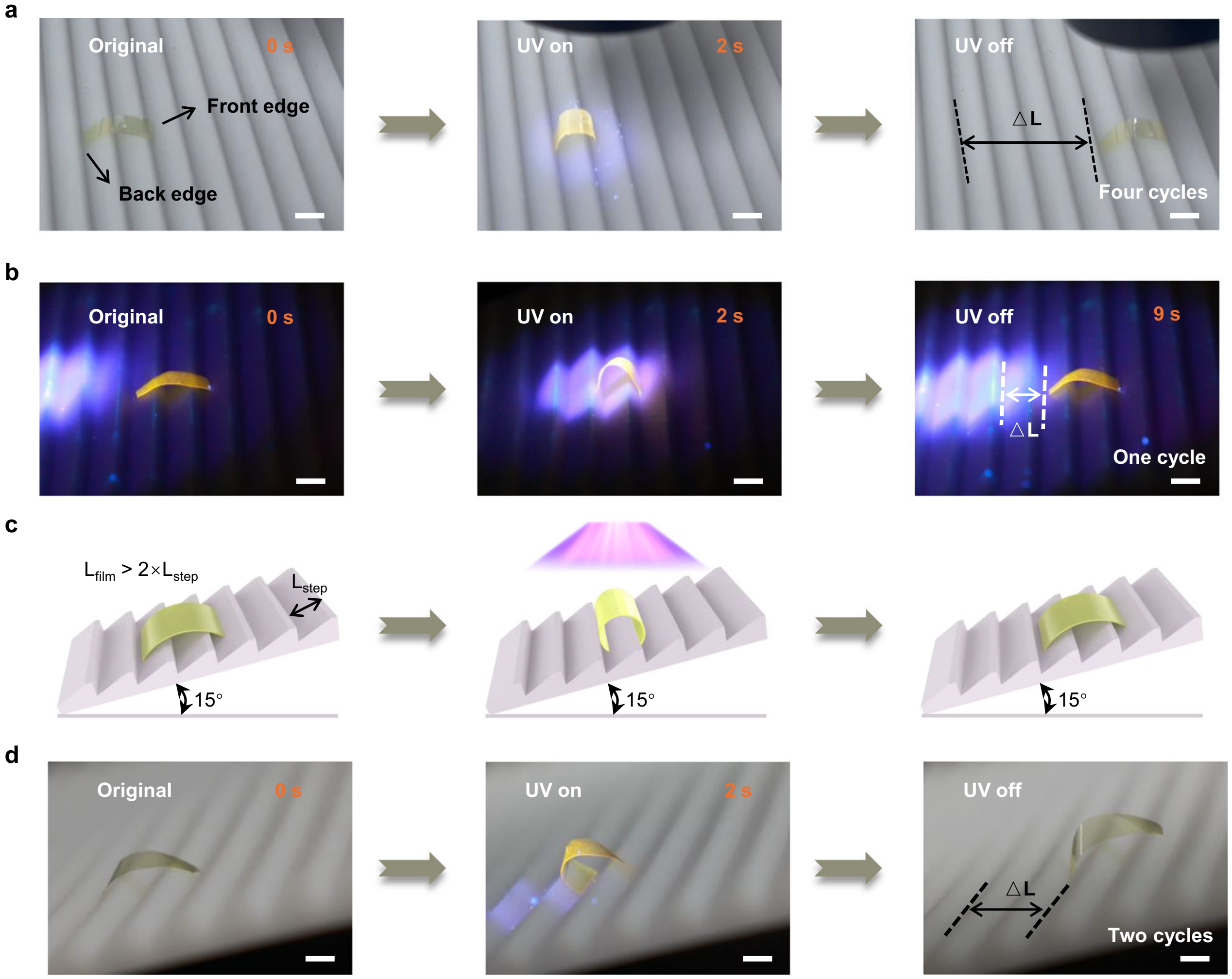

Fig. 4 | Crawling of a walking robot being triggered by UV light. a Photographs of 6FDA-PI based walking robot crawling forward on a ratcheted substrate upon on–off UV light illumination cycles. Scale bars, 6 mm. **b** Photographs of TPE-PI based walking robot crawling forward on a ratcheted substrate in the darkness upon turning on and off UV light. Scale bars, 6 mm. **c** Schematic illustration of walking robot. **d** Photographs of TPE-PI based walking robot crawling up a ratcheted substrate at a 15° incline in response to on and off cycles of UV light. Scale bars, 6 mm.

significantly increased. In addition, the driving properties of actuators (thickness 10 μm) under different light intensities were investigated. As shown in Supplementary Figs. 44 and 45, weak UV light at 50 mW cm^{-2} could also trigger the bending of a film, where the bending angle reached 90° in approximately 4.02 s. Further increasing the light intensity to 100 mW cm^{-2} improved the response speed of the actuator, allowing it to bend 90° in 1.45 s. By increasing the light intensity to 150 and 200 mW cm^{-2}, the actuator could bend 90° in 0.59 s and 0.43 s, respectively. Compared to the reported azobenzene-containing PIs that showed slow response time and needed the operation of dual wavelength (UV and visible light) for reversible actuation[26,37], the actuating performance of PIs is significantly improved. Besides, we added some experiments to demonstrate that our proposed strategy could also easily prepare actuators responsive to infrared light. As shown in Supplementary Fig. 46a, one side of the actuator was painted black with a marker pen, and it was found that under the light irradiation of 808 nm, the film could undergo reversible actuation. This simple strategy can further achieve the response of multi-wavelength lights in one material. As shown in Supplementary Fig. 46b, the right side of a long strip of actuator was blackened with a marker while leaving the left side untreated. When 808 nm light was irradiated on the right side of the film, reversible actuation occurred due to the photothermal effect of the black film, while the left part of the film could not be driven by irradiation due to the non-absorption of infrared light. However, when the entire film was exposed to UV light (Supplementary Fig. 46c), reversible driving occurred throughout the film.

Photoresponsive soft robots enable miniaturization without the need for external batteries and can be controlled remotely. Given that the flexibility and the bending behavior of the actuator when irradiated by different intensity of UV light, we successfully used a UV flashlight to make the actuator crawl as a soft walking robot. Figure 4a shows the 6FDA-PI robot crawling forward on a ratcheted substrate upon on-off UV light illumination cycles (Supplementary Movie 2). The length of the robot (L_{film}) is finely tuned to be slightly longer than that of two steps (L_{step}) of the ratcheted substrate. Upon irradiation with UV light, the robot underwent downward bending. The front edge of the film acted as a stationary end due to the ratcheted substrate surface while the back edge was unencumbered and moved forward about one step. When the UV light was removed, the unbending force generated by the decrease in temperature returned the robot to its original shape. At that moment the back edge became a stationary end, allowing the front edge of the film to extend forward about one step. Repeating this process enables the robot to quickly and continuously walk on the substrate at a speed of about 24 mm min^{-1}, moving forward about one step each time the light is turned on and off, which is about half the distance of its own length. Besides, the construction of multifunctional actuators is highly desirable. Due to the introduction of TPE, a single UV light is able to stimulate color change and deformation of actuator simultaneously. In darkness, the robot remains invisible. Upon UV illumination, TPE-PI film is visible and generates fluorescence, allowing robot to achieve synchronous location tracking while crawling. Once UV light moves away from the robot, the yellow emission disappears and the robot completely hides in darkness again (Fig. 4b and Supplementary Movie 3). Importantly, our robot is also capable of crawling up a ratcheted substrate at a 15° incline in response to on and off cycles of UV light (Fig. 4c, d and Supplementary Movie 4). The integration of these fantastic properties gives a great potential for application of detection and search.

As mentioned earlier, TPE-PI exhibits remarkable UV-activated fluorescence capability, allowing for the creation of high-resolution fluorescence patterns on silicon substrates. More interestingly, fluorescent information of different patterns and letters can also be encrypted on free-standing TPE-PI film using photomasks by UV light (Fig. 5a). When a TPE-PI film covered by photomask with a 2D AIE-style letter was exposed to 365 nm UV light for 10 min, the AIE pattern was effectively encrypted onto the film. The encrypted letters are not visible in daylight but can be clearly read under UV light (Fig. 5b), exhibiting the potential for product anticounterfeiting and information security. Similarly, the flower-style pattern can also be easily encrypted on the film, except for using a different photomask (Fig. 5c). Importantly, the encrypted information can be erased after a long period of direct UV light irradiation of the film, during which the long exposure leads to the fact that weak fluorescence intensity of the original film gradually increases to a high saturation level, which is comparable with the fluorescence intensity of the exposure area, thus leading to the disappearance of information (Fig. 5c). That is to say, using our PI film as a "paper", a single UV light can encrypt information as a "pencil", decrypt information, and erase information as an "eraser". It is worth mentioning that while encrypting information, a gradient spatial distribution along the thickness direction is also established, resulting in a patterned photoactuator (Fig. 5a). When this actuator is exposed to UV light again, it can not only display the previously encrypted fluorescent pattern, but also perform reversible actuation. These synergistic properties make the functionality of our smart photoactuator similar to those observed in intelligent living organisms. For example, when stimulated by invaders, mimic octopuses simultaneously change their shape and exhibit patterns on their bodies to mimic poisonous anemone, thereby achieving the goal of transmitting threatening information (Fig. 5d). Once the threat

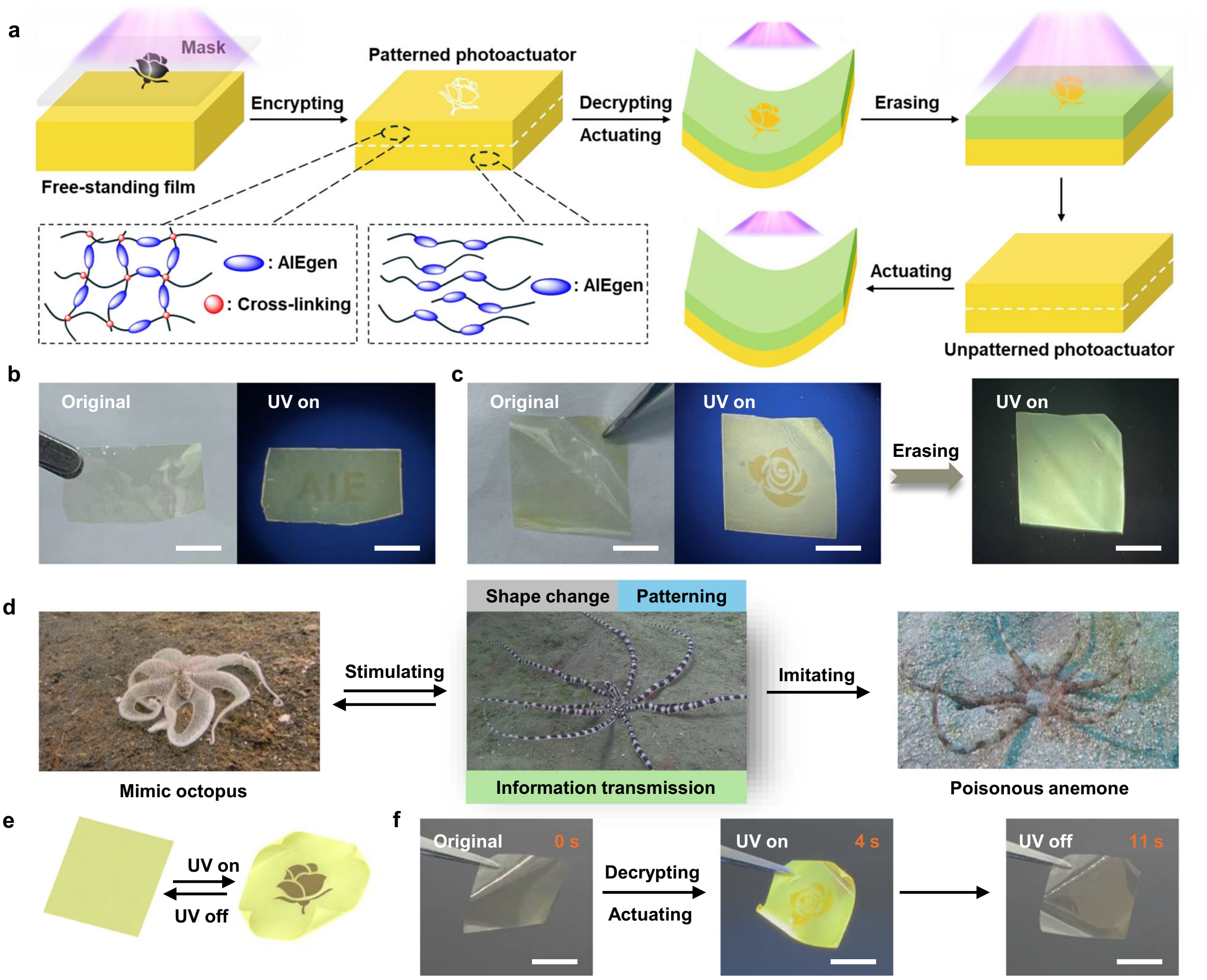

Fig. 5 | Designing the patterned and unpatterned photoactuators. a Schematic illustration of the fabrication and actuation of patterned and unpatterned photoactuators. **b** Encryption of AIE-style letter on the TPE-PI film, which is invisible under daylight but can be recognized under UV light. Scale bars, 10 mm. **c** Encryption and erasure of flower-style pattern on the TPE-PI film. Scale bars, 10 mm. **d** Mimic octopus changing shape and displaying patterns to mimic poisonous anemone when stimulated. **e** Schematic illustration of patterned actuator upon turning on and off the UV light. **f** Photographs of patterned actuator simultaneously showing reversible actuation and exhibiting pattern upon turning on and off the UV light. Scale bars, 10 mm.

subsides, the mimic octopuses return to their initial unpatterned appearance. As shown in Fig. 5e, f, the original shape of the smart actuator without stimulation remains stretched and transparent. Upon UV stimulation, the actuator not only performs motion but also display a fluorescence pattern, achieving dynamic information transmission (Supplementary Movie 5). This is highly consistent with the functionality exhibited by the threatened mimic octopus. When the UV light is removed, the actuator returns to its initial state, with this transition being reversible upon on-off UV light illumination. Similarly, the encrypted information on the actuator can also be erased with UV light, thus resulting in an unpatterned photoactuator (Fig. 5a). Light-driven 3D actuation combined with the encryption and erasure of fluorescent messages establish a dynamic "dimension" for high security encryption beyond traditional 2D and 3D encryption. This example implies that we have developed a straightforward strategy using just UV light to achieve PI films information encryption, spatial distribution, fast reversible motion, information reading and information erasure all in one, greatly simplifying the fabrication of high-performance multi-function intelligent actuators.

The functionality described above is based on UV illumination of the entire film. Given that the spatiotemporal control of photocrosslinking can be achieved through various means, here we also demonstrated the flexibility of our method in selectable gradient inscription in PI film, achieving more complex shape morphing. As shown in Fig. 6a, when using light to selectively irradiate the right half of the front surface and the left half of the back surface of the film, a

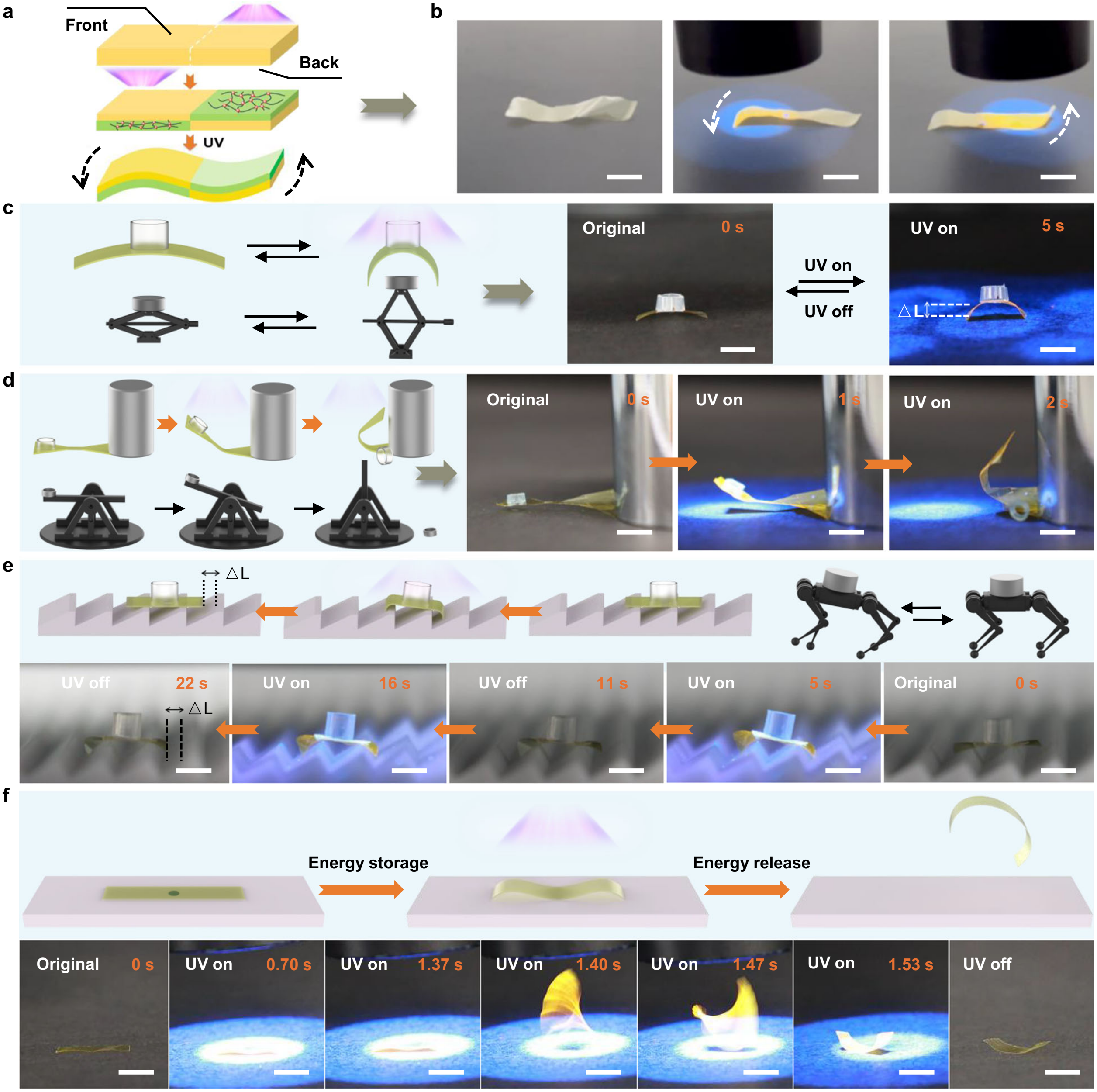

Fig. 6 | Photoactuators with complex deformation and potential mechanical applications. a Schematic illustration of 6FDA-PI film showing optically selectable gradient inscription. **b** Photographs showing the actuator performing different motions when stimulated at different locations. Scale bars, 10 mm. **c** Schematic illustration (left) and photographs (right) of 6FDA-PI film showing the ability of weightlifting. Scale bars, 10 mm. **d** Schematic illustration (left) and photographs (right) of 6FDA-PI film showing the ability of throwing object. Scale bars, 10 mm. **e** Schematic illustration (top) and photographs (bottom) of 6FDA-PI film showing the ability of transporting object. Scale bars, 10 mm. **f** Schematic illustration of the jumping mechanism (top) and photographs (bottom) of 6FDA-PI film jumping through releasing stored elastic energy. Scale bars, 15 mm.

well-defined spatial distribution is achieved with the front surface of the right half is crosslinked while the back surface retains linear structure. On the contrary, the cross-linking of the left half is generated on the back surface, while the front retains linear structure. Such unique spatial distribution caused the chosen regions of a film exhibiting different deformations upon irradiation. As shown in Fig. 6b, UV exposure on the film's left section induced a downward bending attributed to a larger expansion at the front compared to the back. Progressively shifting the UV light to the right restored the left edge to its original form, while further movement towards the right section caused the right edge to bend upwards due to the larger expansion at the back. After removing the light, the entire film returned to its initial shape. Quickly moving UV light from left to right imparted a wavy-like motion to the film due to the instantaneous fast response (Supplementary Movie 6). Thanks to the strong mechanical properties of PI matrix, we investigated its ability to directly convert light energy into a substantial amount of mechanical work as photomechanical materials for the valuable application of mechanical engineering. Figure 6c illustrates a scissor jack, a lifting mechanism typically employed for lifting and supporting heavy objects. Remarkably, our photoactuator, with a mere thickness of 10 µm, is capable of elevating loads 30 times its own weight in only 5 s, akin to a scissor jack, allowing for wireless and remote operations (Supplementary Movie 7). Notably, the photoactuator also serves as a catapult, throwing objects placed on one end of the dumbbell-type film upon UV exposure within 2 s (Fig. 6d), leveraging the high mechanical properties of the PI matrix. This process is repeatable. (Supplementary Movie 8). Moreover, we explored the potential of actuator as load-bearing robot for object transportation. Figure 6e shows the crawling process of an actuator loaded with 30 times its own weight on a ratcheted substrate (Supplementary Movie 9). These cases prove that the prepared actuators exhibit great prospects in future engineering applications, but enhanced load capacity and broader application scenarios are still the goals to be overcome. Furthermore, achieving leaping like grasshoppers and frogs in polymer materials is both fascinating and exceedingly rare[52–54]. The PI actuator reported here also demonstrates its leaping capability, benefiting from a combination of mechanical rigidity and rapid actuation. The center of the irradiated side of film is gently adhered to the substrate using a trace amount of adhesive (Fig. 6f). Upon exposure to UV light, the original film is split into two parts proceeding downward-driving motion, with the center immobilized by the adhesive. With increasing exposure time, elastic strain energy gradually accumulates, eventually causing the film to detach from the adhesive. The release of stored elastic energy results in the film leaping from the substrate (Supplementary Movie 10). While demonstrating the jumping ability of light-driven janus PI film, achieving directional, stable leaping independent of other materials still requires substantial efforts to make engineering applications feasible.

Discussion

In summary, an efficient, mild, and straightforward catalyst-free thiol-yne click polymerization was developed to access photosensitive PI films. The selective non-uniform spatial distribution of the PI films, the rapid reversible complex deformation of the actuators, and the encryption, reading, and erasing of information on the actuator were easily achieved by using just UV light, without the need for film orientation. Thanks to the robust mechanical property and driving ability, light energy can still be converted into obvious motion, even under heavy loads. Our work has established crucial design guidelines for improving the performance of future actuators. Firstly, we demonstrated that a "janus" strategy of single material provided a simple and effective approach for reversible actuators, and the fast motion of the actuators was not contradictory to the mechanical robustness of the material. Secondly, more mild and efficient methods still need to be developed to prepare functional polymers containing photosensitive units, extending beyond photolithography to the fabrication of diverse photomechanical materials with heterogeneity. Finally, our strategy highlights the intrinsic value of light. Using single UV light can achieve the integration of plentiful functions into PIs. It is foreseeable that polymers capable of selectively responding to multiple wavelengths of light and an expanded material diversity will lead to more advanced multifunctional actuators, eschewing the need of batteries and focusing on miniaturization, which will benefit the progress in microrobotics and bionic manufacturing.

Methods

Materials

3-Aminophenylacetylene (APA, 98.0%), 4-aminothiophenol (97.0%), γ-terpinene (95.0%), phthalic anhydride (99.0%), anhydrous potassium carbonate (98.0%), 4-nitrophthalonitrile (98.0%), potassium hydroxide (95.0%), 4,4′-(Hexafluoroisopropylidene)diphthalic anhydride (6FDA, 98.0%) and 4,4′-(4,4′-isopropylidenediphenoxy)bis-(phthalic anhydride) (BPADA, 97.0%) were purchased from Macklin. 4,4′-(1,2-diphenylethene-1,2-diyl)diphenol (97.0%) was purchased from Bidepharm (Shanghai). Tetrahydrofuran (THF, 99.9%), ethanol (>95.0%), dimethyl sulfoxide (DMSO, >99.7%), acetic acid (HOAc, >99.5%), cyclohexane (>99.7%), acetic anhydride (>98.5%) and hydrochloride acid (36.0–38.0 %) were purchased from Sigma-Aldrich and used without further purification.

Characterizations

Nuclear magnetic resonance (NMR) measurements were carried out on a Bruker Avance 400 spectrometer in deuterated solvents (DMSO-d_6 or $CDCl_3$). Fourier transform infrared spectroscopy (FT-IR) spectra were recorded on an FT-IR spectrophotometer (Bruker Tensor 27). Mass spectra were measured on a WATERS I-Class VION IMS QTof Mass Spectrometer (LC-TOF-MS) in an electrospray ionization (ESI)-positive mode. The molecular weight of PIs was obtained with gel permeation chromatography (GPC, HLC 8020) by using tetrahydrofuran (THF, 0.5 mL/min) as eluent solvent. Polystyrene standards were used for calibration of the GPC. UV-Vis measurements were conducted on a PerkinElmer LAMBDA 365 spectrophotometer. Thermal gravimetric analyses (TGA) were performed on a Mettler Toledo TGA2 synchronous thermal analyzer at a heating rate of 10 °C min^{-1} in nitrogen from 30 °C to 800 °C. The glass transition temperature (T_g) of PI films were measured on a DMA 850 instrument at a heating rate of 2 °C min^{-1} at a frequency of 1 Hz in a tensile mode. The curves of thermal expansion of PI films were measured on a TMA 450 instrument at a heating rate of 5 °C min^{-1} and a nitrogen flow rate of 50 mL min^{-1}. Wide angle X-ray diffraction (WAXD) measurements were carried out on the Bruker D8 Advance (Bruker, Germany). Differential scanning calorimetry (DSC) was done in a DSC3 (Mettler-Toledo) equipment at a heating rate of 10 °C min^{-1} under a nitrogen atmosphere. The mechanical properties (ultimate tensile strength, elongation at break and tensile modulus) were tested on three to five rectangular film strips according to ASTM D882-88 at a crosshead speed of 2 mm/min at ambient temperature. The tensile modulus is taken as the initial slope of the stress–strain curves. The mechanical properties were reported as average values on at least three samples. The refractive indices of the PI films were measured on a J. A. Woollam Variable Angle Ellipsometer with a model of Alpha-SE and a wavelength tunability from 370 to 1690 nm. Photoluminescence (PL) spectra of films and solutions were recorded on an Edinburgh FLS1000 Spectrofluorometer. The thin films were prepared by spin-coating the 1,2-dichloroethane solutions (~20 mg/mL) on silicon wafers at 1000 rpm for 1 min and then dried in a vacuum oven at room temperature. The photoirradiation process of the films was conducted in air at room temperature using UV light (100 mW cm^{-2}). SEM images were recorded on the TESCAN Mira3 field emission SEM instrument. Change of fluorescence intensity upon irradiation time was conducted with a confocal laser scanning microscope (Leica TCS SP8 STED 3X, wavelength: 405 nm). Photographs were taken using a Nikon D5100 digital camera. The thermographs were taken by a Flir E76 infrared (IR) thermal imaging camera (FLIR, USA).

Synthetic procedures of dithiol monomer 1 (6FSH)

The dithiol (6FSH) was prepared by the routes shown in Supplementary Fig. 1. 6FDA (10 mmol, 4.4424 g) and 4-aminothiophenol (20 mmol, 2.5038 g) were added to a 250 mL round flask. Then 150 mL of HOAc and 30 mL of cyclohexane were added to flask and the mixture was stirred at 130 °C for 6 h. Water was continuously removed using a Dean-Stark trap. Then the mixture was cooled to room temperature and poured slowly into 500 mL of ice cooled H_2O to produce a yellow precipitate. The precipitate was filtered and washed several times with H_2O, followed by drying under vacuum at 80 °C for 12 h. (6.25 g, 95% yield). ^{1}H-NMR (400 MHz, 25 °C), δ ($CDCl_3$, ppm): 8.04 (d, J = 8.0 Hz, 4H, Ar-H),7.88-7.91 (m, 4H, Ar-H), 7.41 (d, J = 8.5 Hz, 4H, Ar-H), 7.30 (d, J = 8.5 Hz, 4H, Ar-H), 3.56 (s, 2H, -SH). ^{13}C-NMR (100 MHz, 25 °C), δ ($CDCl_3$, ppm): 166.07, 165.90, 139.26, 136.02, 132.70, 132.40, 132.15, 129.95, 128.90, 127.11, 125.47, 124.89, 124.26, 122.03, 65.31. FT-IR (KBr, cm^{-1}): 3478, 3094, 2551, 1777, 1714, 1498, 1436, 1380, 1295, 1245, 1212, 1191, 1149, 1095, 960, 873, 823, 719. ESI-MS (m/z): calcd for $[M+H]^+$: 659.05284, found: $[M+H]^+$: 659.05343.

Synthetic procedures of diyne monomers 2 (6FDA-APA), 3 (BPADA-APA) and 4 (TPE-APA)

6FDA-APA: 6FDA (10 mmol, 4.4424 g) and APA (2.343 g, 20 mmol) were added to a 250 mL round flask. Then 100 mL of HOAc and 20 mL of cyclohexane were added to flask and the mixture was stirred at 130 °C for 6 h. Water was continuously removed using a Dean-Stark trap. Then the mixture was cooled to room temperature and poured slowly into 500 mL of ice cooled H_2O to get a white precipitate. The precipitate was filtered and washed several times with H_2O, followed by drying under vacuum at 80 °C for 12 h. (5.97 g, 93 % yield). ^{1}H-NMR (400 MHz, 25 °C), δ ($CDCl_3$, ppm): 8.06 (d, 2H, Ar-H), 7.94 (s, 2H, Ar-H), 7.89 (d, 2H, Ar-H), 7.57–7.42 (m, 8H, Ar-H), 3.14 (s, 2H, ≡CH). ^{13}C-NMR (101 MHz, 25 °C), δ (DMSO-d_6, ppm): 166.4, 166.2, 137.9, 136.4, 133.5, 133.0, 132.4, 132.00, 130.9, 129.9, 128.6, 124.9, 124.2, 122.9, 82.9, 82.2, 65.1. FT-IR (KBr, cm^{-1}): 3282, 1783, 1721, 1483, 1435, 1369, 1254, 1197, 1147, 1100, 716. ESI-MS (m/z): calcd for $[M + Na]^+$: 665.09065, found: $[M + Na]^+$: 665.09116.

BPADA-APA: BPADA (5.2049 g, 10 mmol) and APA (2.343 g, 20 mmol) were added to a 250 mL round flask. Then 100 mL of HOAc and 20 mL of cyclohexane were added to flask and the mixture was stirred at 130 °C for 6 h. Water was continuously removed using a Dean-Stark trap. Then the mixture was cooled to room temperature and poured slowly into 500 mL of ice cooled H_2O to get a white precipitate. The precipitate was filtered and washed several times with H_2O, followed by drying under vacuum at 80 °C for 12 h. (6.61 g, 92 % yield). ^{1}H-NMR (400 MHz, 25 °C), δ ($CDCl_3$, ppm): 7.90 (d, 2H, Ar-H), 7.57 (s, 2H, Ar-H), 7.51 (d, 2H, Ar-H), 7.47–7.33 (m, 12H, Ar-H), 7.04 (d, 2H, Ar-H), 3.12 (s, 2H, ≡CH), 1.76 [s, 6H, $C(CH_3)_2$]. ^{13}C-NMR (101 MHz, 25 °C), δ (DMSO-d_6, ppm): 166.4, 163.4, 152.9, 147.6, 134.5, 132.6, 131.6, 130.6, 129.8, 129.1, 128.2, 126.4, 125.6, 123.3, 122.8, 120.2, 111.9, 83.0, 82.2, 42.5, 31.0. FT-IR (KBr, cm^{-1}): 3280, 1729, 1717, 1607, 1479, 1435, 1373, 1276, 1219, 1100, 1074, 850. ESI-MS (m/z): calcd for $[M + Na]^+$: 741.19961, found: $[M + Na]^+$: 741.19948.

TPE-APA was synthesized by the routes depicted in Supplementary Fig. 2.

Intermediate ***i***. 4,4′-(1,2-diphenylethene-1,2-diyl)diphenol (1.09 g, 3 mmol), 4-nitrophthalonitrile (1.04 g, 6 mmol), and anhydrous potassium carbonate (K_2CO_3) (0.83 g, 6 mmol) were added to 50 mL dimethyl sulfoxide (DMSO) solution, followed by stirring at room temperature for 24 h in a nitrogen atmosphere. The solid was filtered, washed with water for three times and dried under vacuum at 80 °C for 12 h (1.80 g, 97% yield). ^{1}H-NMR (400 MHz, 25 °C), δ (DMSO-d_6, ppm): 8.12 (d, J = 8.8 Hz, 1H, Ar-H), 8.02 (d, J = 8.8 Hz, 1H, Ar-H), 7.63 (s, 1H, Ar-H), 7.53 (s, 1H, Ar-H), 7.32–6.98 (m, 20H, Ar-H).

Intermediate ***ii***. The intermediate ***i*** (0.90 g, 1.5 mmol) was dispersed in 10 mL of ethanol. Then a solution of KOH (1.16 g, 20.0 mmol) dissolved in 10 mL of H_2O was added dropwise. The system was stirred at 110 °C for 12 h, followed by cooling to room temperature and acidifying with HCl (6 M) to adjust the pH between 1 and 2 to produce a white precipitate. The precipitate was filtered and washed several times with H_2O until the filtrate was neutral, followed by drying at 100 °C under vacuum for 12 h. (0.97 g, 94% yield). ^{1}H-NMR (400 MHz, 25 °C), δ (DMSO-d_6, ppm): 13.38 (s, 4H, -COOH), 7.80 (s, 2H, Ar-H), 7.22–6.90 (m, 22H, Ar-H).

Intermediate ***iii***. The tetracarboxylic acid intermediate ***ii*** (0.70 g, 1 mmol) was added to 30 mL of acetic anhydride, followed by stirring at 120 °C for 12 h. Then the mixture was cooled to room temperature and a yellow solid was precipitated in acetic anhydride. The precipitate was filtered and washed several times with acetic anhydride, followed by drying under vacuum at 120 °C for 12 h (0.63 g, 96% yield). ^{1}H-NMR (400 MHz, 25 °C), δ (DMSO-d_6, ppm): 8.09 (d, J = 8.4 Hz, 1H, Ar-H), 7.98 (d, J = 8.4 Hz, 1H, Ar-H), 7.47 (t, 2H, Ar-H), 7.28–7.00 (m, 20H, Ar-H).

TPE-APA ***iv***. intermediate ***iii*** (0.46 g, 0.7 mmol) and APA (0.16 g, 1.4 mmol) were added to a 150 mL round flask. Then 30 mL of HOAc and 6 mL of cyclohexane were added to flask and the mixture was stirred at 130 °C for 10 h. Water was continuously removed using a Dean–Stark trap. Then the mixture was cooled to room temperature and poured slowly into 100 mL of ice cooled H_2O to get a white precipitate. The precipitate was filtered and washed several times with H_2O, followed by drying under vacuum at 80 °C for 12 h. (0.57 g, 95 % yield). ^{1}H-NMR (400 MHz, 25 °C), δ ($CDCl_3$, ppm): 7.90–7.70 (m, 4H, Ar-H), 7.58–7.13 (m, Ar-H), 7.05–7.00 (m, 4H, Ar-H), 3.14–3.13 (2H, ≡CH). ^{13}C-NMR (100 MHz, 25 °C), δ ($CDCl_3$, ppm): 166.55, 166.51, 166.24, 166.03, 164.59, 163.91, 153.30, 153.25, 143.10, 142.75, 141.65, 141.03, 140.82, 140.67, 134.24, 133.83, 133.62, 133.40, 131.99, 131.87, 131.77, 131.65, 131.43, 131.39, 130.16, 129.86, 129.25, 129.19, 128.16, 128.06, 127.20, 127.09, 126.77, 125.93, 125.78, 125.08, 124.41, 123.37, 123.33, 123.26, 120.64, 119.89, 111.91, 110.71, 82.72, 78.48, 78.44. FT-IR (KBr, cm^{-1}): 3283, 3073, 1777, 1722, 1599, 1502, 1478, 1430, 1371, 1278, 1224, 1102, 850, 744, 702, 628. ESI-MS (m/z): calcd for $[M+H]^+$: 855.2417, found: $[M+H]^+$: 855.2495.

Preparation of model compound

The synthesis of model compound is outlined in Supplementary Fig. 3. **Intermediate *i*.** Phthalic anhydride (1.4811 g, 10 mmol) and APA (1.1715 g, 10 mmol) were added to a 150 mL round flask. Then 50 mL of HOAc and 10 mL of cyclohexane were added to flask and the mixture was stirred at 130 °C for 6 h. Water was continuously removed using a Dean-Stark trap. Then the mixture was cooled to room temperature and poured slowly into 50 mL of ice cooled H_2O to get a white precipitate. The precipitate was filtered and washed several times with H_2O, followed by drying under vacuum at 80 °C for 12 h. (2.40 g, 97% yield). ^{1}H-NMR (400 MHz, 25 °C), δ ($CDCl_3$, ppm): 7.97–7.95 (m, 2H, Ar-H),7.81–7.79 (m, 2H, Ar-H), 7.60–7.59 (m, 1H, Ar-H), 7.53–7.45 (m, 3H, Ar-H), 3.13 (s, 1H, ≡CH).

Model Compound. Intermediate ***i*** (0.7417 g, 3.0 mmol) and p-thiocresol (0.3726 g, 3.0 mmol) were added to 20 mL of THF taken in a 50 mL Schlenk tube in a nitrogen atmosphere, followed by. stirring at 30 °C for 12 h. Then THF was removed under reduced pressure to get a yellow solid product, followed by purifying by a silica gel column chromatography. (0.78 g, 70 % yield). ^{1}H NMR (400 MHz, 25 °C), δ ($CDCl_3$, ppm): 7.98-7.94 (m, 2H, Ar-H), 7.81_7.79 (m, 2H, Ar-H), 7.60–7.28 (m, 6H, Ar-H), 7.16 (d, J = 8.0 Hz, 2H, Ar-H), 6.93–6.51 (m, 2H, =C-H), 2.35 (s, 3H, $-CH_3$). FT-IR (KBr, cm^{-1}): 1777, 1706, 1597, 1490, 1465, 1426, 1381, 1284, 1234, 1179, 1109, 1078, 944, 873, 802, 785, 745, 707, 678.

Polyimide synthesis

A typical procedure for the polymerization of **1** and **2** is given as an example. **1** (0.8891 g, 1.35 mmol) and **2** (0.8674 g, 1.35 mmol) were added to 9 mL of THF taken in a 50 mL three-necked flask equipped with a mechanical agitation in a nitrogen atmosphere, followed by stirring at 30 °C for 15 min to afford a viscous PI solution. Then 10 mL of THF was added and the solution was poured slowly into 300 mL ethanol to give yellowish fibrous precipitate. The precipitate was filtered and washed three times with ethanol (1.63 g, 93% yield). The mechanism exploration of this polymerization was performed under similar procedures except that the radical trapper, *γ*-terpinene, was added to the system.

Characterization data 6FDA-PI (1 + 2). $M_w = 108$ kDa, PDI = 2.68. ^{1}H-NMR (400 MHz, 25 °C), *δ* ($CDCl_3$, ppm): 8.04–7.89 (m, 12H, Ar-*H*), 7.60-7.32 (m, 16H, Ar-*H*), 6.97–6.80 (= C-*H* from the *E*-vinylene unit), 6.68–6.58 (= C-*H* from the *Z*-vinylene unit). FT-IR (KBr, cm^{-1}): 3069, 3036, 1785, 1723, 1600, 1494, 1432, 1370, 1297, 1251, 1193, 1145, 1101, 962, 719.

Characterization data for BPADA-PI (1 + 3). $M_w = 126$ kDa, PDI = 2.48. ^{1}H-NMR (400 MHz, 25 °C), *δ* ($CDCl_3$, ppm): 8.05–7.87 (m, 8H, Ar-*H*), 7.58–7.32 (m, 24H, Ar-*H*), 7.04 (d, *J* = 8.0 Hz, 4H, Ar-*H*), 6.96–6.80 (= C-*H* from the *E*-vinylene unit), 6.67-6.56 (= C-*H* from the *Z*-vinylene unit). FT-IR (KBr, cm^{-1}): 3648, 3482, 3065, 2971, 2684, 1779, 1716, 1598, 1496, 1434, 1369, 1235, 1147, 1075, 1014, 960, 844, 784, 721.

Characterization data for TPE-PI (1 + 4). $M_w = 67$ kDa, PDI = 2.30. ^{1}H-NMR (400 MHz, 25 °C), *δ* ($CDCl_3$, ppm): 8.03-7.88 (m, 6H, Ar-*H*), 7.69–6.93 (m, Ar-*H*), 6.85 (= C-*H* from the *E*-vinylene unit), 6.68–6.57 (= C-*H* from the *Z*-vinylene unit). FT-IR (KBr, cm^{-1}): 3642, 3485, 3059, 1729, 1724, 1600, 1495, 1476, 1442, 1366, 1230, 1145, 1099, 1016, 962, 847, 721.

Polymer and monomer film formation

PI powders (0.2 g) were well dissolved in DMAc (2 wt%), followed by filtration through a nylon membrane with 0.22 µm pore size to remove any insoluble impurities. Then the solution was cast onto a levelled glass disc, followed by slowly evaporating the solvent in vacuum at 80 °C for 10 h, heated to 100, 120, 140, and 160 °C, and held at these temperatures each for 2 h to afford a PI thin film with thickness of 5–20 µm. The TPE-APA thin film was prepared by spin-coating the dichloromethane solutions of TPE-APA (~20 mg/mL) on silicon wafers at 1000 rpm for 1 min. The PMMA was dissolved in dichloromethane solution and prepared into 18 wt% solution, followed by dissolving TPE-APA monomer in the solution (~20 mg/mL) and spin-coating on silicon wafers at 1000 rpm for 1 min to obtain TPE-APA /PMMA film.

Photopatterning

Photo-crosslinking of the PI films were conducted in air at room temperature using 365 nm light with intensity of 100 mW cm^{-2}. The films were firstly prepared by spin-coating the polymer solution (~20 mg/mL) on silicon wafers at 1000 rpm for 1 min and then dried in a vacuum oven at room temperature. The 2D patterns were generated by UV irradiation of the films through copper photomasks with different sizes and shapes for 20 min, followed by development in 1,2-dichloroethane to obtain 3D patterns.

Fabrication of actuators

The actuators were easily obtained by placing the free-stranding PI films (~10 µm) under the UV lamp (365 nm, 100 mW cm^{-2}) and irradiating the front side for 30 min. Patterned actuators were obtained by irradiating a free-standing TPE-PI film (~10 µm) through copper photomask with pattern using an UV lamp for 30 min (365 nm, 100 mW cm^{-2}). The obtained patterned actuator was irradiated with UV light under a transparent glass plate for 12 h to eliminate the fluorescent patterns, thus producing unpatterned actuator. The actuator with complex shape morphing was obtained by illumination of the front side of the right half of the film, followed by illumination of the back surface of the left half.

Data availability

The data of this study are provided in the Supplementary Information and Source Data file. Source data are provided with this paper. Additional data are available from the corresponding author upon request. Source data are provided with this paper.

References

1. Ni, C. et al. Shape memory polymer with programmable recovery onset. *Nature* **622**, 748–753 (2023).
2. Li, Z. et al. Bioinspired simultaneous changes in fluorescence color, brightness, and shape of hydrogels enabled by AIEgens. *Adv. Mater.* **32**, 1906493 (2020).
3. Gelebart, A. H. et al. Making waves in a photoactive polymer film. *Nature* **546**, 632–636 (2017).
4. Kim, Y., Yuk, H., Zhao, R., Chester, S. A. & Zhao, X. Printing ferromagnetic domains for untethered fast-transforming soft materials. *Nature* **558**, 274–279 (2018).
5. Xu, W. et al. Photo-actuators via epitaxial growth of microcrystal arrays in polymer membranes. *Nat. Mater.* **22**, 1152–1159 (2023).
6. Kim, S.-U. et al. Broadband and pixelated camouflage in inflating chiral nematic liquid crystalline elastomers. *Nat. Mater.* **21**, 41–46 (2022).
7. Ge, F. & Zhao, Y. Microstructured actuation of liquid crystal polymer networks. *Adv. Funct. Mater.* **30**, 1901890 (2020).
8. Palleau, E., Morales, D., Dickey, M. D. & Velev, O. D. Reversible patterning and actuation of hydrogels by electrically assisted ionoprinting. *Nat. Commun.* **4**, 2257 (2013).
9. Huang, Y. et al. Bioinspired synergistic photochromic luminescence and programmable liquid crystal actuators. *Angew. Chem. Int. Ed.* **60**, 11247–11251 (2021).
10. Palagi, S. et al. Structured light enables biomimetic swimming and versatile locomotion of photoresponsive soft microrobots. *Nat. Mater.* **15**, 647–653 (2016).
11. Arazoe, H. et al. An autonomous actuator driven by fluctuations in ambient humidity. *Nat. Mater.* **15**, 1084–1089 (2016).
12. Deng, J. et al. Tunable photothermal actuators based on a pre-programmed aligned nanostructure. *J. Am. Chem. Soc.* **138**, 225–230 (2016).
13. Herbert, K. M. et al. Synthesis and alignment of liquid crystalline elastomers. *Nat. Rev. Mater.* **7**, 23–38 (2022).
14. Guin, T. et al. Layered liquid crystal elastomer actuators. *Nat. Commun.* **9**, 2531 (2018).
15. Zeng, H., Wasylczyk, P., Wiersma, D. S. & Priimagi, A. Light robots: bridging the gap between microrobotics and photomechanics in soft materials. *Adv. Mater.* **30**, 1703554 (2018).
16. Zeng, H., Wani, O. M., Wasylczyk, P., Kaczmarek, R. & Priimagi, A. Self-regulating iris based on light-actuated liquid crystal elastomer. *Adv. Mater.* **29**, 1701814 (2017).
17. Pei, Z. et al. Mouldable liquid-crystalline elastomer actuators with exchangeable covalent bonds. *Nat. Mater.* **13**, 36–41 (2014).
18. Lu, X. et al. Liquid-crystalline dynamic networks doped with gold nanorods showing enhanced photocontrol of actuation. *Adv. Mater.* **30**, 1706597 (2018).
19. Wie, J. J., Shankar, M. R. & White, T. J. Photomotility of polymers. *Nat. Commun.* **7**, 13260 (2016).
20. Chen, G. et al. Rapidly and repeatedly reprogrammable liquid crystalline elastomer via a shape memory mechanism. *Adv. Mater.* **34**, 2201679 (2022).

21. Fang, M. et al. Ultrafast digital fabrication of designable architectured liquid crystalline elastomer. *Adv. Mater.* **33**, 2105597 (2021).
22. Yang, R. & Zhao, Y. Non-uniform optical inscription of actuation domains in a liquid crystal polymer of uniaxial orientation: an approach to complex and programmable shape changes. *Angew. Chem. Int. Ed.* **56**, 14202–14206 (2017).
23. Kosa, T. et al. Light-induced liquid crystallinity. *Nature* **485**, 347–349 (2012).
24. Lahikainen, M., Zeng, H. & Priimagi, A. Reconfigurable photoactuator through synergistic use of photochemical and photothermal effects. *Nat. Commun.* **9**, 4148 (2018).
25. Jiang, Z.-C., Xiao, Y.-Y., Tong, X. & Zhao, Y. Selective decrosslinking in liquid crystal polymer actuators for optical reconfiguration of origami and light-fueled locomotion. *Angew. Chem. Int. Ed.* **58**, 5332–5337 (2019).
26. Sun, X., Zhang, M., Wei, J. & Yu, Y. Multiple shape manipulation of azobenzene-containing polyimide by combining shape memory effect, photofixity, and photodeformation. *ACS Macro Lett* **12**, 921–927 (2023).
27. Pang, X., Lv, J.-a, Zhu, C., Qin, L. & Yu, Y. Photodeformable Azobenzene-containing liquid crystal polymers and soft actuators. *Adv. Mater.* **31**, 1904224 (2019).
28. Zhang, X. et al. Photoactuators and motors based on carbon nanotubes with selective chirality distributions. *Nat. Commun.* **5**, 2983 (2014).
29. Ma, S., Li, X., Huang, S., Hu, J. & Yu, H. A light-activated polymer composite enables on-demand photocontrolled motion: transportation at the liquid/air interface. *Angew. Chem. Int. Ed.* **58**, 2655–2659 (2019).
30. Song, T. et al. Supramolecular hydrogen bond enables Kapton nanofibers to reinforce liquid-crystalline polymers for light-fueled flight. *Nano Energy* **87**, 106207 (2021).
31. Wang, J., Yang, B., Yu, M. & Yu, H. Light-powered self-sustained oscillators of graphene oxide/liquid crystalline network composites showing amplitude and frequency superposition. *ACS Appl. Mater. Inter.* **14**, 15632–15640 (2022).
32. Chen, D. et al. Orthogonal photochemistry toward direct encryption of a 3D-printed hydrogel. *Adv. Mater.* **35**, 2209956 (2023).
33. Ren, Y.-Y. et al. A smart single-fluorophore polymer: self-assembly shapechromic multicolor fluorescence and erasable ink. *Adv. Mater.* **35**, 2307971 (2023).
34. Zhang, J. et al. Stimuli-responsive AIEgens. *Adv. Mater.* **33**, 2008071 (2021).
35. Chen, X. et al. In-situ controllable synthesis of carbon dots for patterned fluorescent wood films rapid fabrication strategy. *Aggregate* **5**, e519 (2024).
36. Lu, H.-F., Wang, M., Chen, X.-M., Lin, B.-P. & Yang, H. Interpenetrating liquid-crystal polyurethane/polyacrylate elastomer with ultrastrong mechanical property. *J. Am. Chem. Soc.* **141**, 14364–14369 (2019).
37. Wang, D. H., Wie, J. J., Lee, K. M., White, T. J. & Tan, L.-S. Impact of backbone rigidity on the photomechanical response of glassy, azobenzene-functionalized polyimides. *Macromolecules* **47**, 659–667 (2014).
38. Wie, J. J., Wang, D. H., Lee, K. M., Tan, L.-S. & White, T. J. Molecular engineering of Azobenzene-functionalized polyimides to enhance both photomechanical work and motion. *Chem. Mater.* **26**, 5223–5230 (2014).
39. Lee, K. M. et al. Enhancement of photogenerated mechanical force in Azobenzene-functionalized polyimides. *Angew. Chem. Int. Ed.* **51**, 4117–4121 (2012).
40. Baczkowski, M. L. et al. Photomechanical deformation of azobenzene-functionalized polyimides synthesized with bulky substituents. *ACS Macro Lett* **6**, 1432–1437 (2017).
41. Ge, F., Lu, X., Xiang, J., Tong, X. & Zhao, Y. An optical actuator based on gold-nanoparticle-containing temperature-memory semicrystalline polymers. *Angew. Chem. Int. Ed.* **56**, 6126–6130 (2017).
42. Fu, X., Qin, A. & Tang, B. Z. X-yne click polymerization. *Aggregate* **4**, e350 (2023).
43. He, B. et al. Polymerizations of activated alkynes. *Prog. Polym. Sci.* **126**, 101503 (2022).
44. Xue, S. et al. Highly refractive polyimides derived from efficient catalyst-free Thiol–Yne click polymerization. *Macromolecules* **54**, 11256–11268 (2021).
45. Han, T. et al. Photoresponsive spiro-polymers generated in situ by C–H-activated polyspiroannulation. *Nat. Commun.* **10**, 5483 (2019).
46. Cai, Y. et al. Deciphering the working mechanism of aggregation-induced emission of tetraphenylethylene derivatives by ultrafast spectroscopy. *Chem. Sci.* **9**, 4662–4670 (2018).
47. Wang, J. et al. Z/E effect on phase behavior of main-chain liquid crystalline polymers bearing AIEgens. *Macromolecules* **54**, 10740–10749 (2021).
48. Li, J. et al. Recent advances in flexible self-oscillating actuators. *eScience* **4**, 100250 (2024).
49. Yu, Y. et al. Fiber-shaped soft actuators: fabrication, actuation mechanism and application. *Adv. Fiber Mater.* **5**, 868–895 (2023).
50. Li, J. et al. Photothermal Bimorph actuators with in-built cooler for light mills, frequency switches, and soft robots. *Adv. Funct. Mater.* **29**, 1808995 (2019).
51. Li, J. et al. High performance and multifunction moisture-driven Yin–Yang-interface actuators derived from Polyacrylamide Hydrogel. *Small* **19**, 2303228 (2023).
52. Hebner, T. S., Korner, K., Bowman, C. N., Bhattacharya, K. & White, T. J. Leaping liquid crystal elastomers. *Sci. Adv.* **9**, eade1320 (2023).
53. Hu, J. et al. Springtail-inspired light-driven soft jumping robots based on liquid crystal elastomers with monolithic three-leaf panel fold structure. *Angew. Chem. Int. Ed.* **62**, e202218227 (2023).
54. Guo, H., Ruoko, T.-P., Zeng, H. & Priimagi, A. Hydrogen-bonded liquid crystal elastomers combining shape memory programming and reversible actuation. *Adv. Funct. Mater.* **34**, 2312068 (2024).

Acknowledgements

This work was financially supported by the National Natural Science Foundation of China (52273197, Z.Z.; 52333007, B.Z.T.; 52203144, S.N.; 22275148, Q.Z.), National Key Research and Development Program of China (2023YFB3810001, Z.Z.), Shenzhen Key Laboratory of Functional Aggregate Materials (ZDSYS20211021111400001, B.Z.T.), the Science Technology Innovation Commission of Shenzhen Municipality (KQTD20210811090142053, B.Z.T.; JCYJ20220818103007014, B.Z.T.; GJHZ20210705141810031, Z.Z.; JCYJ2021324134613038, Z.Z.), the Fundamental Research Funds for the Central Universities (G2022KY05103, J.Z.). We would like to thank the Analytical & Testing Center of Northwestern Polytechnical University.

Author contributions

Q.Z., B.Z.T., Z.Z., J.Z., and S.X. conceived the concept and wrote the paper. S.X. carried out the majority of the experiments and tests with help from Z.S., Z.W., H.T., F.G., Z-C.Z., Z.Y., S.N., and T.H. All authors discussed the results.

Competing interests

The authors declare no competing interests.

Additional information

Supplementary information The online version contains supplementary material available at https://doi.org/10.1038/s41467-024-54386-9.

Correspondence and requests for materials should be addressed to Jianbo Zhang, Zheng Zhao, Ben Zhong Tang or Qiuyu Zhang.

Peer review information *Nature Communications* thanks Zunfeng Liu, Haifeng Yu, and the other, anonymous, reviewer(s) for their contribution to the peer review of this work. A peer review file is available.

Reprints and permissions information is available at http://www.nature.com/reprints

Publisher's note Springer Nature remains neutral with regard to jurisdictional claims in published maps and institutional affiliations.

Open Access This article is licensed under a Creative Commons Attribution-NonCommercial-NoDerivatives 4.0 International License, which permits any non-commercial use, sharing, distribution and reproduction in any medium or format, as long as you give appropriate credit to the original author(s) and the source, provide a link to the Creative Commons licence, and indicate if you modified the licensed material. You do not have permission under this licence to share adapted material derived from this article or parts of it. The images or other third party material in this article are included in the article's Creative Commons licence, unless indicated otherwise in a credit line to the material. If material is not included in the article's Creative Commons licence and your intended use is not permitted by statutory regulation or exceeds the permitted use, you will need to obtain permission directly from the copyright holder. To view a copy of this licence, visit http://creativecommons.org/licenses/by-nc-nd/4.0/.

© The Author(s) 2024